Intermetallics 155 (2023) 107832

Contents lists available at ScienceDirect

Intermetallics

journal homepage: www.elsevier.com/locate/intermet

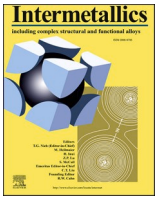

The scratch characteristics of laser nitrided Zr-based metallic glass surface

Jing Hong [a], Haoxiang Wu [a], Hu Huang [a,*], Lin Zhang [b], Zhiyu Zhang [c], Minqiang Jiang [d,e], Jiwang Yan [b]

[a] Key Laboratory of CNC Equipment Reliability, Ministry of Education, School of Mechanical and Aerospace Engineering, Jilin University, Changchun, Jilin, 130022, China
[b] Department of Mechanical Engineering, Faculty of Science and Technology, Keio University, Yokohama, 223-8522, Japan
[c] Key Laboratory of Optical System Advanced Manufacturing Technology, Changchun Institute of Optics, Fine Mechanics and Physics, Chinese Academy of Sciences, Changchun, China
[d] State Key Laboratory of Nonlinear Mechanics, Institute of Mechanics, Chinese Academy of Sciences, Beijing, 100190, China
[e] School of Engineering Science, University of Chinese Academy of Sciences, Beijing, 100049, China

ARTICLE INFO

Keywords:
Metallic glass
Laser processing
Tribological properties
Mechanical properties
Scratch

ABSTRACT

Improving the surface hardness and tribological characteristics of metallic glasses (MGs) is meaningful for their applications as surface contact materials. In this study, nanosecond laser nitriding was performed on Zr-based MG to improve its surface properties. Three types of laser nitrided surfaces with different hardness were prepared, and their tribological characteristics were systematically investigated by means of the scratch test. The experimental results indicated that compared with the as-cast MG, the hardness of these three laser nitrided surfaces was increased by 47.94%, 114.56%, and 171.99%, and their coefficients of friction were reduced by 29.12%, 65.05%, and 71.84%, respectively. Furthermore, the residual scratches and surrounding chips exhibited various features under different conditions, and the scratch damage mechanisms were analyzed accordingly.

1. Introduction

Metallic glasses (MGs) benefit from the long-range disordered structure and thereby exhibit exceptional mechanical, physical and chemical properties, such as high elasticity, low modulus of elasticity, excellent soft magnetic property and corrosion resistance [1–4]. In particular, compared with many crystalline alloys, the relatively superior hardness and wear resistance provide potential applications for MGs in the preparation of bearing rollers, defense weapons and medical instruments [5–8]. For extending the range of applications and satisfying the actual service conditions, it is essential to further improve the surface properties of MGs.

Surface modification technologies such as deposition or spraying [9–12] are generally employed to improve the surface properties of materials. By these methods, the strengthening layer with excellent mechanical and tribological characteristics could be introduced on the material substrate. However, due to the difference in intrinsic properties between the substrate and the strengthening layer, the adhesion strength at the interface is difficult to guarantee. Thus, the fracture and delamination induced by fatigue are prone to occur under high-stress conditions. Fortunately, the advances in laser technologies including laser nitriding [13–16], laser cladding [17–20], and laser carburizing [21–23] have offered new opportunities in the field of surface modification. Among these technological methods, laser nitriding is identified as an effective method due to the advantages of convenient operation and environmental friendliness. In some previous studies [13,14], laser nitriding has been performed on the Zr-based MG surface. During laser nitriding, due to the chemical affinity of nitrogen and zirconium elements under high temperature condition, ZrN phase could be generated in situ and embedded into the substrate to form a nitrided layer, significantly enhancing the surface hardness of Zr-based MG. However, the effects of laser nitriding on the tribological characteristics of Zr-based MG have not been investigated yet.

In this study, by laser nitriding, three types of laser nitrided Zr-based MG surfaces with different surface hardness were prepared. Then, the tribological characteristics (the coefficient of friction (COF), residual scratches and chips) of these laser nitrided surfaces were systematically investigated by scratch tests. The experimental results indicated that compared with the as-cast MG, the COFs of these three laser nitrided surfaces were reduced by 29.12%, 65.05%, 71.84% respectively, and

* Corresponding author.
E-mail address: huanghu@jlu.edu.cn (H. Huang).

https://doi.org/10.1016/j.intermet.2023.107832
Received 19 November 2022; Received in revised form 4 January 2023; Accepted 15 January 2023
Available online 19 January 2023

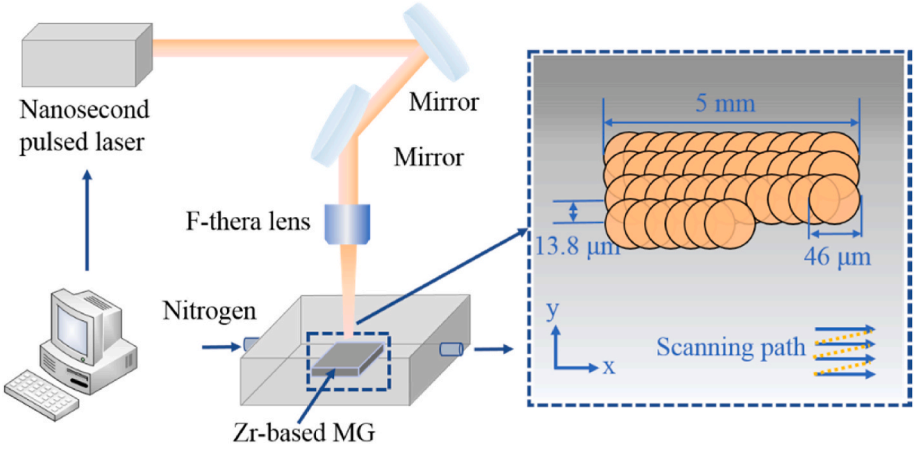

Fig. 1. The schematic of the laser irradiation system for preparing the laser nitrided surfaces under nitrogen atmosphere.

Table 1
Laser nitriding parameters corresponding to each case.

	Laser power (W)	Scanning speed (mm/s)	Track overlap (%)	Number of irradiation cycle
Case 1	3.6	10	70	1
Case 2	3.6	10	70	2
Case 3	3.6	10	70	3

narrower residual scratches were obtained correspondingly. Furthermore, the scratch damage mechanisms under different conditions were analyzed. To further identify the differences in scratch damage mechanisms between the as-cast MG and laser nitrided surfaces, the cross-sectional analysis was performed as well.

2. Materials and experiments

2.1. Laser nitriding process

A typical Zr-based MG block ($Zr_{41.2}Ti_{13.8}Cu_{12.5}Ni_{10}Be_{22.5}$) with a dimension of 20 mm × 20 mm × 2 mm was commercially available. The specimen was ground with a series of sandpapers (400, 800, 1500, 2000, and 3000) to obtain a smooth surface, and then cleaned with acetone. To obtain the laser nitrided surface, the specimen was placed in a nitrogen-filled cavity, and then irradiated by a fiber nanosecond pulsed laser (SP–050P-A-EP-Z-F-Y, SPI Lasers, UK). This system emits near-infrared light with a Gaussian energy distribution, and the central wavelength, pulse width, and repetition frequency are 1064 nm, 10 ns, and 600 kHz, respectively. The schematic of the laser irradiation system is illustrated in Fig. 1, where the laser beam is focused on the MG surface with a focal length of 160 mm using a F-theta lens and scanned by a computerized numerical control system. According to the previous study [14], the degree of laser nitriding depends on the laser parameters such as the laser power, scanning speed, track overlap between two neighboring scanning tracks, and number of irradiation cycle. To obtain the laser nitrided surfaces with various surface hardness, three kinds of number of irradiation cycles were employed (1, 2, and 3), and the laser power, scanning speed and track overlap were selected as 3.6 W, 10 mm/s and 70%, respectively, as listed in Table 1. Thus, three laser nitrided surfaces (cases 1–3) with the processed area of 4 mm × 4 mm were obtained. To guarantee the comparability of experimental results, laser nitriding experiments were performed on the identical specimen.

2.2. Nanoindentation and scratch tests

It is recognized that nanoindentation is an effective method for assessing the mechanical characteristics of materials at the micro/nano-scale [24–27]. Accordingly, the nanoindentation instrument (DUH-211S, SHIMADZU, Japan) with a pyramidal indenter was employed to measure the hardness of the as-cast MG and laser nitrided surfaces. This indenter has an angle of 115° between the ridge and face. During the nanoindentation process, the load and penetration depth of the indenter are recorded. By analyzing the recorded data using the Oliver-Pharr method [28], the surface hardness could be obtained. For the nanoindentation tests, the maximum indentation load, loading rate, and load holding time were selected as 120 mN, 10 mN/s, and 5 s, respectively. To reduce the test error, the nanoindentation tests were repeated 10 times for each case. For characterizing the tribological characteristics of the as-cast MG and laser nitrided surfaces, a self-made

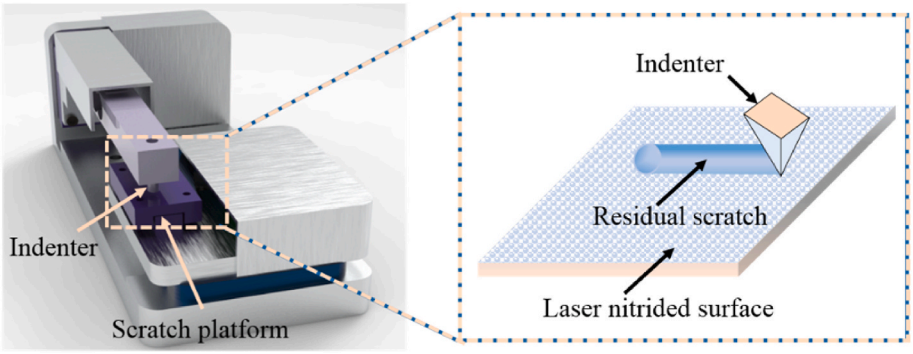

Fig. 2. Schematic diagram illustrating the scratch test on the laser nitrided surface.

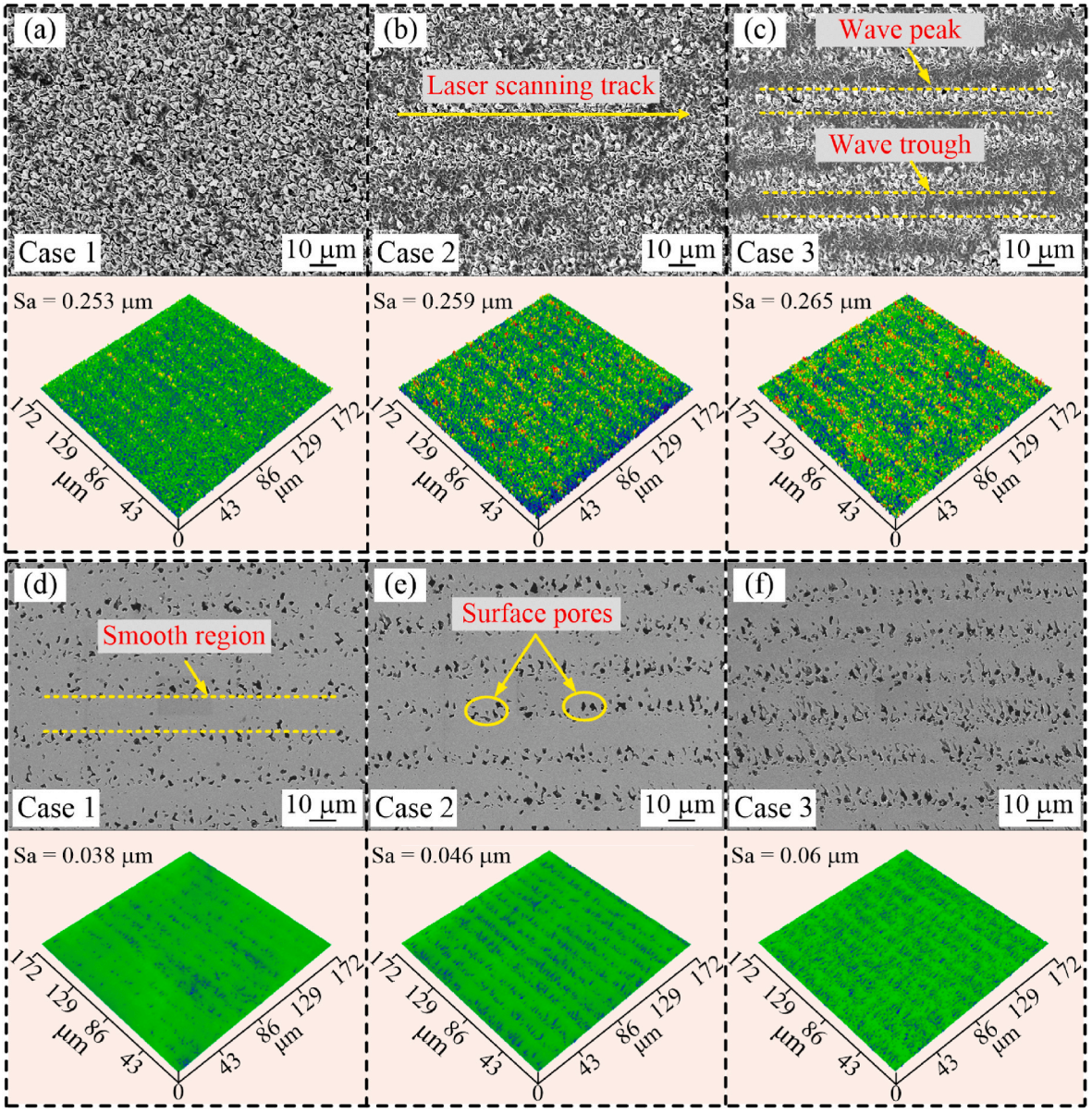

Fig. 3. SEM micrographs and 3D topographies of the laser nitrided surfaces: (a) case 1, (b) case 2, and (c) case 3. SEM micrographs and 3D topographies of the laser nitrided surfaces after mechanical polishing: (d) case 1, (e) case 2, and (f) case 3.

scratch test system equipped with a diamond Vickers indenter was used, and its schematic diagram is shown in Fig. 2. Prior to the scratch tests, the specimen was fixed on the scratch platform. During the scratch tests, the scratch platform was moved relative to the indenter at a speed of 20 μm/s, and the normal and tangential loads were measured. The normal loads used for the scratch tests were selected as 50, 100, 200, 300, 400, and 500 mN.

2.3. Characterization methods

The micrographs of the laser nitrided surfaces, residual indentations, residual scratches as well as chips generated during scratch were observed by the tungsten filament scanning electron microscope (SEM, JSM-IT500A, JEOL, Japan). The applied voltage and working distance were 10.0 kV and 10.0 mm, respectively. For characterizing the phases of the laser nitrided surfaces, an X-ray diffractometer (XRD, D8 Discover, Bruker, Germany) was used. Phase identification was performed with the 2θ angle between 20° and 80°. In addition, the three-dimensional (3D) topographies of the laser nitrided surfaces and residual scratches were measured by the laser scanning confocal microscope (LSCM, OLS4100, Olympus, Japan).

3. Results and discussion

3.1. Morphology analysis of laser nitrided surfaces

Fig. 3 presents the SEM micrographs and 3D topographies of the Zr-based MG surfaces treated by laser nitriding under the parameters listed in Table 1. It is observed that for all the three laser nitrided surfaces, apparent material ablation is generated. Especially for case 3, wave peaks and troughs along the laser scanning track are observed (Fig. 3(a)-3(c)). This is because under the irradiation of high-energy laser beam, vaporization of surface materials may occur, leading to the generation of the recoil pressure. Under the action of recoil pressure, the materials of the irradiated region are pushed outward until they are blocked by the previous laser scanning track, finally forming the wave peaks and troughs. The formation of the surface defects aforementioned would lead to an increase in surface roughness of laser nitrided surfaces, which

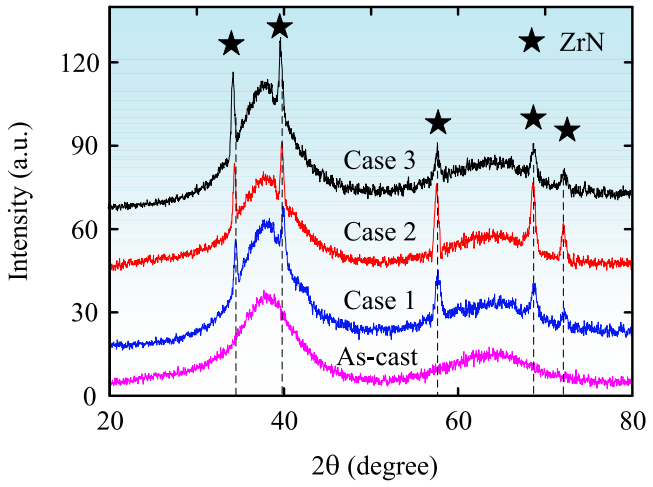

Fig. 4. XRD patterns of the as-cast MG as well as laser nitrided surfaces after mechanical polishing.

in turn affects the subsequent nanoindentation and scratch tests. Therefore, mechanical polishing was performed on the cases 1, 2, and 3 surfaces to reduce the surface roughness. Simultaneously, to minimize the effect of mechanical polishing on the nitrided layer, the thickness of the material removal layer during mechanical polishing was controlled to be less than the values between wave peaks and wave troughs of the laser nitrided surfaces. Accordingly, the surface roughness of the laser nitrided surfaces has been remarkably reduced from 0.253, 0.259, and 0.265 μm to 0.038, 0.046, and 0.06 μm, and some surface pores appear as illustrated in Fig. 3(d)-3(f). These surface pores are relatively evenly distributed and could act like the micro dimples in surface texturing. In addition, the laser nitrided surfaces after mechanical polishing were characterized by XRD and the results are presented in Fig. 4. Only one broad diffraction peak is detected around 2θ of 38° on the XRD pattern of the as-cast MG, demonstrating its amorphous feature [29–31]. While for cases 1–3 surfaces, the obvious diffraction peaks of ZrN phase are detected, and the peak intensity is increased from case 1 to case 3 [32]. This indicates that the content of ZrN phase generated during laser nitriding is enhanced by increasing the number of irradiation cycle.

3.2. Nanoindentation characteristics

To assess the strengthening effect of laser nitriding on the as-cast MG surface, all specimens were subjected to nanoindentation measurements. Specifically, the hardness of the as-cast MG and cases 1–3 surfaces was calculated by data processing software included in the nanoindentation instrument, which is based on the Oliver-Pharr (OP) method. The involved equation is given by $H = P_{max}/A$, where H and P_{max} stand for the nanoindentation hardness and the maximum indentation load, respectively. A represents an area function that predicts the contact area between the indentation and the surface to be measured. The results, obtained from ten indentations for each specimen, show that all the three laser nitrided surfaces possess much higher hardness than that of the as-cast MG (6.32 GPa), as displayed in Fig. 5(a). Besides, the surface hardness gradually increases from case 1 to case 3, which can be directly seen from the load-depth curves in Fig. 5(b) and the residual indentations in Fig. 5(c), where the maximum indentation depth and the size of residual indentation decrease from case 1 to case 3. This variation trend of the surface hardness matches well with that of the peak intensity of ZrN phase in Fig. 4, which indicates that the increase in surface hardness is closely associated with the ZrN phase. According to the previous studies [33–35], the in-situ formed ZrN phase acts as the secondary phase in MG substrate, which could effectively hinder the fast propagation of the main shear band. Accordingly, the resistance to plastic deformation is enhanced, contributing to its surface hardening. On the other hand, the ZrN phase with inherently high hardness is beneficial to further improve the hardness of the irradiated surface. It is noted that evident shear bands are observed around the residual indentation for as-cast MG surface as shown in Fig. 5(b), while they are barely visible on the cases 1–3 surfaces. As mentioned above, the suppression of the main shear band due to the existence of ZrN phase could give a reasonable interpretation for this phenomenon [36]. In general, the above analysis demonstrates that the formation of ZrN phase during

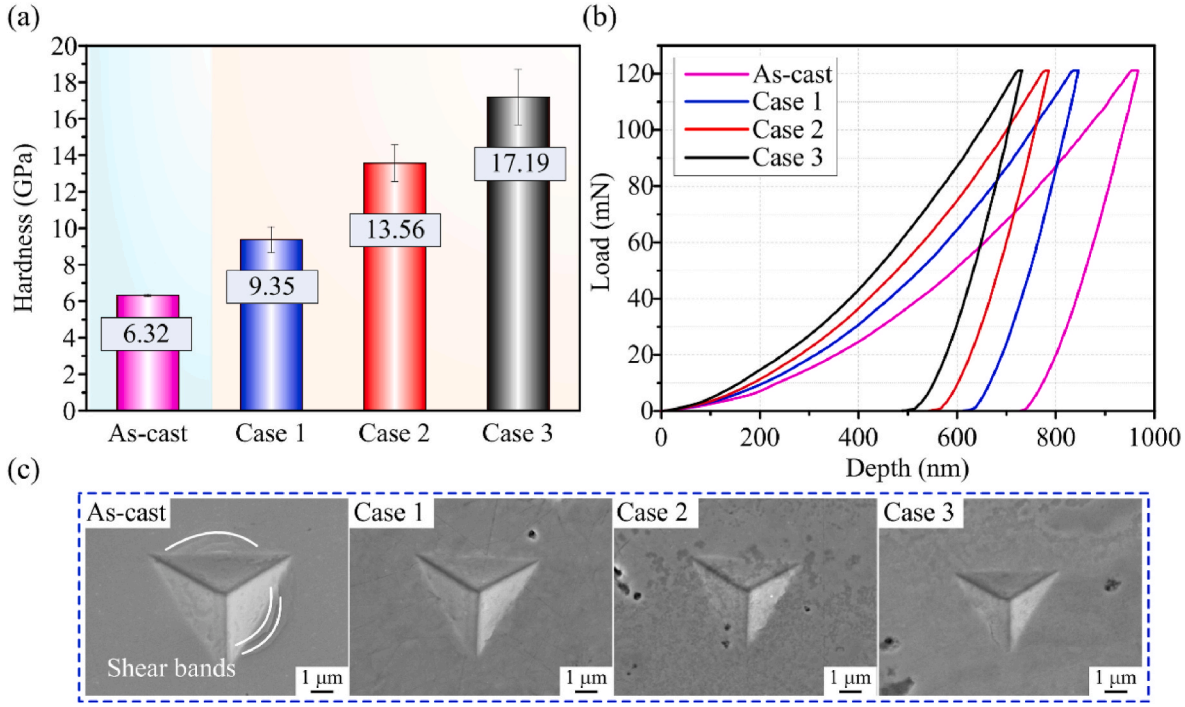

Fig. 5. (a) Surface hardness, (b) load-depth curves and (b) SEM micrographs of residual indentations for as-cast MG as well as cases 1–3.

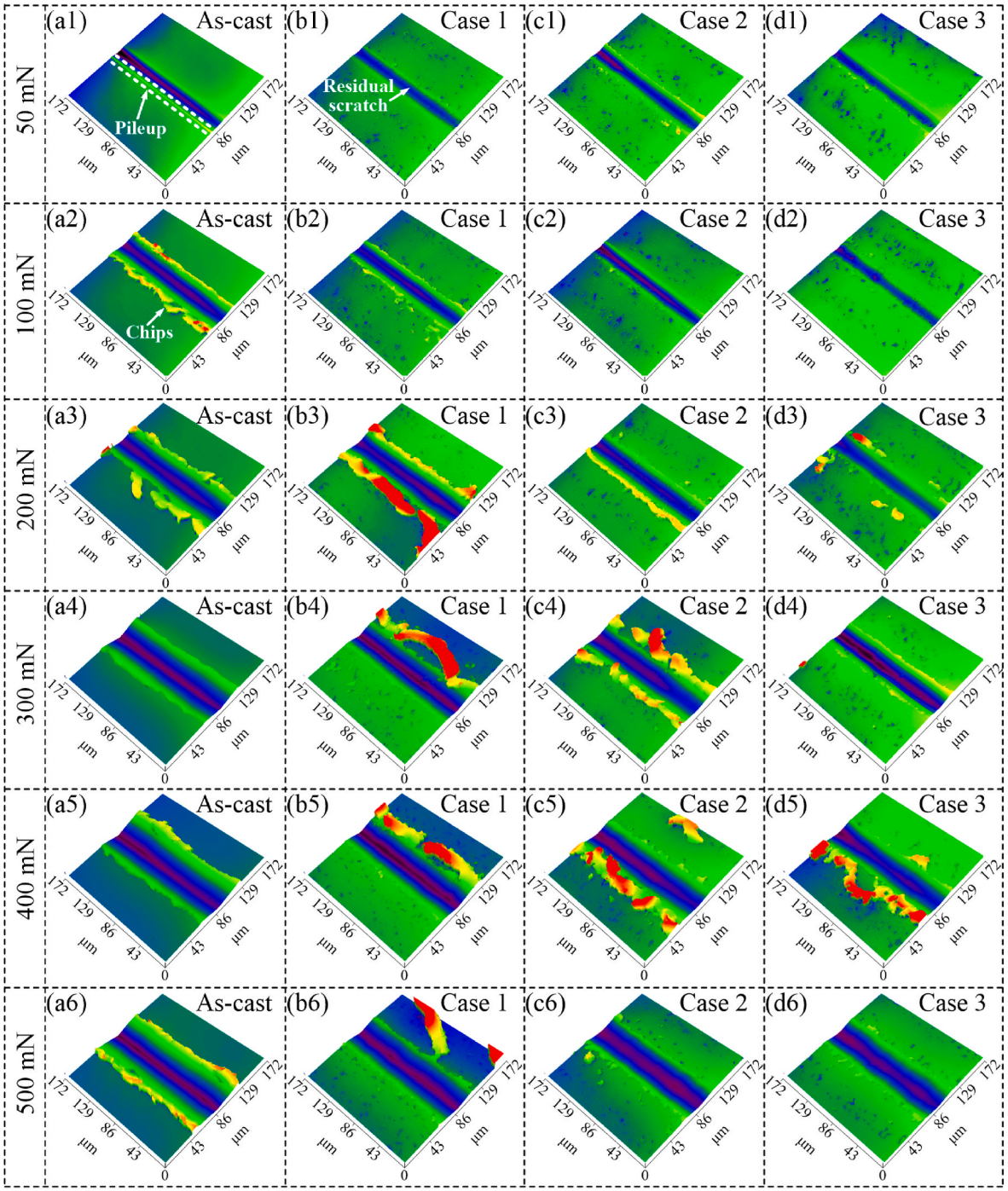

Fig. 6. 3D topographies of the residual scratches on the as-cast MG and cases 1–3 surfaces under various normal loads.

laser nitriding plays a significant role in improving the surface hardness of MG, and more ZrN phase generally leads to higher surface hardness.

3.3. Scratch characteristics

3.3.1. 3D topographies of residual scratches

To evaluate the tribological characteristics of the as-cast MG and cases 1–3 surfaces, scratch tests were performed under the normal loads of 50, 100, 200, 300, 400, and 500 mN. Fig. 6 illustrates the 3D topographies of the scratch regions for the as-cast MG and cases 1–3 surfaces under various normal loads. It is clearly seen that for all the cases, the pileups and chips on both sides of the residual scratches have been generated. For each normal load, the width of the residual scratch on the as-cast MG surface is always greater than those of the cases 1–3 surfaces, which suggests the excellent scratch resistance of the laser nitrided surfaces. Furthermore, from case 1 to case 2, and further to case 3, the width of the residual scratch shows some regular variations. For quantitatively analyzing the widths and depths of these residual scratches, the corresponding cross-sectional profiles are extracted along the direction perpendicular to the residual scratches, as shown in Fig. 7. To reduce the measurement errors, the cross-sectional profiles are extracted from five different locations of each residual scratch, and the average width and depth are obtained and summarized in Fig. 8(a) and (b). It is seen that both the width and depth of the residual scratch exhibit a continuously decreasing trend from the as-cast MG to case 3 under each normal load. Also, the volume loss induced by scratch was measured by

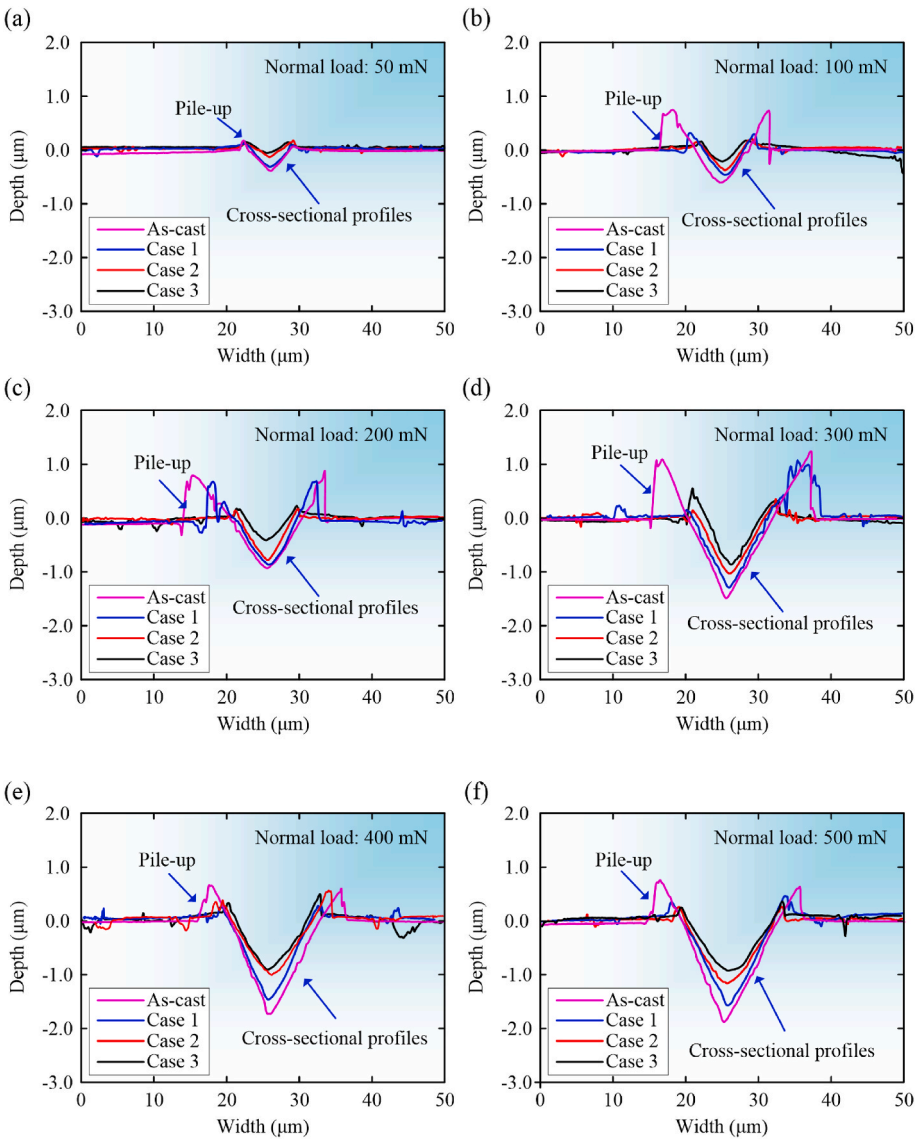

Fig. 7. Cross-sectional profiles of the residual scratches on the as-cast MG and cases 1–3 surfaces under the normal loads of (a) 50 mN, (b) 100 mN, (c) 200 mN, (d) 300 mN, (e) 400 mN, and (f) 500 mN.

LSCM analysis software and presented in Fig. 8(c). Being similar to the aforementioned results, for a given normal load, the as-cast MG always possesses the maximum volume loss, followed by case 1, case 2, and case 3. These observations indicate that the scratch resistance tends to gradually increase with the increase of the number of irradiation cycle. Furthermore, it is noted that the scratch resistance is proportional to the surface hardness in Fig. 5(a). This phenomenon can be explained by the equation $R = H/K$, where R represents the wear resistance coefficient in Pa, H is the hardness in Pa, and K stands for a constant [37].

On the other hand, it is seen that the cross-sectional profiles of the residual scratches possess various features under different conditions as shown in Fig. 7. For the as-cast MG, when increasing the normal load from 50 mN to 300 mN, the width and depth of the cross-sectional profile are remarkably increased. For instance, the width increases from 5.11 μm to 11.80 μm, and the depth increases from 0.40 μm to 1.51 μm. Besides, the height of the pileup on both sides of the corresponding residual scratch increases gradually, as shown in Fig. 7(a)-7(d). As the normal load further increases to 500 mN, the width of the residual scratch presents a milder increasing trend (from 11.80 μm to 12.99 μm) compared with the depth, and the pileup is apparently weakened as shown in Fig. 7(d)-7(f). In comparison, for case 1, case 2, and case 3 surfaces, when the normal load is in the range from 50 mN to 400 mN, the apparent increase in both the width and depth of the cross-sectional profile is observed. For instance, the widths increase from 5.03, 3.44 and 3.30 μm to 12.41, 11.51 and 11.10 μm, and the corresponding depths increase from 0.33, 0.15 and 0.07 μm to 1.49, 0.95 and 0.85 μm, respectively, accompanied by the slight increase in the height of the pileup (Fig. 7(a)-7(e)). When the normal load increases from 400 mN to 500 mN, the widths of the residual scratches present a slight increase (from 12.41, 11.51 and 11.10 μm to 12.95, 12.73 and 12.51 μm, respectively). The above different features may be correlated with different scratch damage mechanisms, which would be discussed later.

3.3.2. SEM morphology and scratch damage mechanism

To analyze the scratch damage mechanism for as-cast MG and cases 1–3 surfaces under the applied normal loads, the SEM micrographs of the residual scratches are shown in Fig. 9. It is observed that the residual scratches with smooth grooves are formed on the as-cast MG and cases 1–3 surfaces under all the normal loads, which exhibits the typical characteristic of abrasive wear. According to some previous studies [38–40], abrasive wear primarily includes three modes, i.e., ploughing, micro-cutting and wedge. Among them, ploughing is mainly beneficial

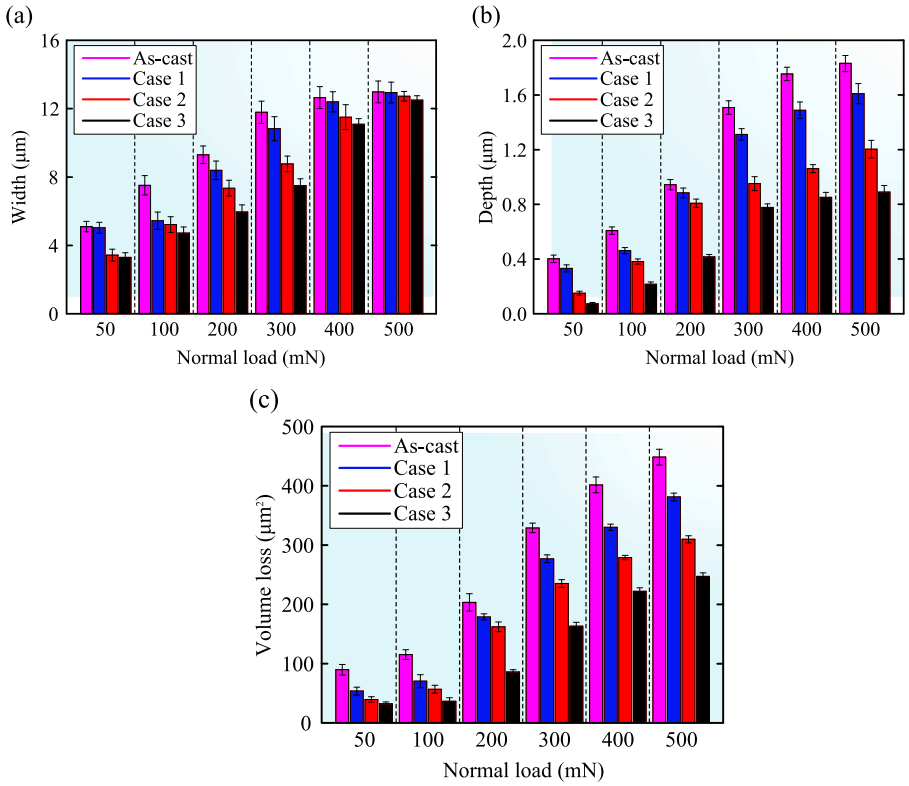

Fig. 8. (a) Widths, (b) depths and (c) volume loss of the residual scratches for as-cast MG, case 1, case 2, and case 3 surfaces under various normal loads.

for the extrusion and accumulation of materials to the sides of the residual scratch [39]. While micro-cutting primarily leads to the removal of materials along the depth direction of the scratch and the formation of chips [41].

For the as-cast MG, when the normal load reaches 50 mN, a narrow groove coupled with the slight pileup is observed (Fig. 9(a1)), which reveals that the principal damage mechanism is ploughing. When increasing the normal load to 100 mN, the penetration depth of the indenter becomes larger, leading to a wider and deeper residual scratch as well as the occurring of chipping events (Figs. 8 and 9(a2)). This indicates that the damage mechanism may have changed from ploughing to the mixed mode of ploughing and micro-cutting. As the normal load increases from 100 mN to 300 mN, both the width and depth of the residual scratch (Fig. 8) increase gradually as well as the height of the pileup (Fig. 7(b)-7(d)), and the segmented or continuous chips are generated (Fig. 9(a2)-9(a4)). This suggests the increasing effects of ploughing and micro-cutting. While, when increasing the normal load from 300 mN to 500 mN, the width of residual scratch shows a moderate increasing trend compared to the corresponding depth (Figs. 8 and 9 (a4)-9(a6)). Besides, the pileup is weakened (Fig. 7(d)-7(f)), and some longer chips are formed and separated from the scratch region (not shown here). This phenomenon could be ascribed to the dominant role of micro-cutting.

Compared with the as-cast MG, the scratch damage for cases 1–3 surfaces is indeed milder in terms of the dimension of the residual scratches as well as the chips and pileups. To further reveal the reasons for the differences in scratch damage, the cross-sectional analyses for cases 1–3 were performed. Specifically, cases 1–3 surfaces were first sectioned by low-speed diamond cutting, and then polished to obtain smooth cross-sections. Then, the SEM micrographs of the cross-sections for cases 1–3 surfaces are illustrated in Fig. 10(a), 10(c), and 10(e), where numerous cluster structures appear, being clearly distinguishable from the MG substrate. To identify the chemical composition evolution induced by laser nitriding, EDS line scanning tests were performed along the depth direction of the cross-sections with the lines 1, 2, and 3 as the measurement originations for cases 1, 2, and 3, respectively. By observing the microstructures in the cross-sections and the distributions of Zr and N elements, it is seen that the depths of the nitrided layer are 6, 13, and 18 μm for case 1, case 2, and case 3, respectively. Further combining the EDS line scanning results (Fig. 10) and the XRD results (Fig. 4), these cluster structures might be the in-situ formed ZrN phase. During scratch, ZrN phase in the MG substrate acts as the load carrying part with the action of normal and tangential forces, which considerably cuts down the direct load subjected by the MG substrate [42], as illustrated in Fig. 11. Therefore, cases 1–3 surfaces have an edge in resisting scratch damage compared to the as-cast MG. On the other hand, plenty of residual surface pores are distributed on the laser nitrided surfaces, as seen in Figs. 3, 6 and 9. These surface pores play a role in reducing the volume of materials around the indenter tip and capturing partial chips [43,44], which may contribute to the further weakening of the scratch damage. To sum up, the evident differences in the scratch damage between the laser nitrided surfaces (cases 1–3) and as-cast MG should arise from the presence of ZrN phase and surface pores. Also, upon the observations on the different distributions of nitrided layers for cases 1–3 in Fig. 10, it is anticipated that these three laser nitrided surfaces could possess some different scratch damage mechanisms. In Fig. 9(b1)-9(d1), the residual scratches obtained under a low normal load of 50 mN reveal that the damage mechanism for cases 1–3 surfaces is ploughing. When increasing the normal load to 100 mN, partial materials in case 1 and case 2 surfaces are squeezed to the sides of the residual scratches to form some scattered debris, accompanied by the continuous increase in the widths and depths of the residual scratches (Figs. 8 and 9(b2)-9(c2)). This indicates their damage mechanism becomes the mixed mode of ploughing and micro-cutting. While for case 3, the damage mechanism still remains the ploughing mode (Fig. 9(d2)), indicating that the transition of its damage mechanism has been delayed. This is primarily due to that the content of ZrN in the MG substrate is apparently increased by tuning the number of irradiation cycle from 1 to 3 (Figs. 4 and 10),

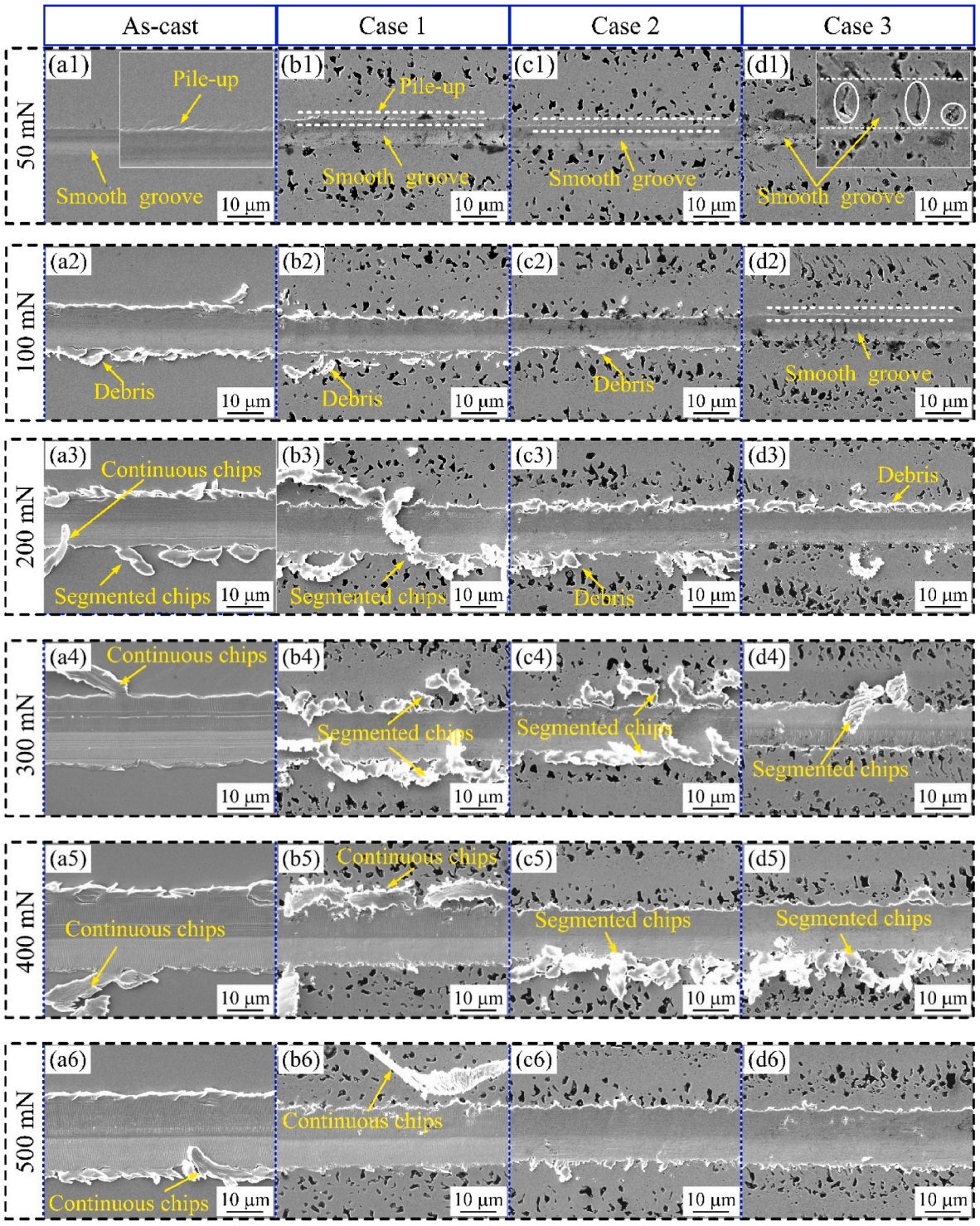

Fig. 9. SEM micrographs of the residual scratches for (a1)-(a6) as-cast MG, (b1)-(b6) case 1, (c1)-(c6) case 2, and (d1)-(d6) case 3 surfaces under the applied normal loads.

resulting in a stronger load-carrying effect for the case 3 surface. Subsequently, the SEM micrographs for cases 1–3 surfaces under the normal loads of 200, 300, and 400 mN suggest that the principal damage mechanism is the mixed mode of ploughing and micro-cutting. When increasing the normal load to 500 mN, the width of residual scratch for case 1 surface basically remains unchanged (Figs. 8 and 9(b6)), and those of case 2 and case 3 surfaces show a moderate increase (Figs. 8 and 9(c6)-9(d6)). Besides, the pileup behavior is alleviated, and the generated chips are separated from the scratch region. This suggests that the micro-cutting may play a dominant role. In general, scratch damage mechanism is not only related to the applied normal load but also to the ZrN phase and surface pores induced by laser nitriding.

In Fig. 9, accompanied by the change of the scratch damage mechanism, the micrographs of the chips exhibit different features as well. Accordingly, the enlarged SEM micrographs of the chips for as-cast MG and cases 1–3 surfaces under two representative normal loads of 200 mN and 400 mN are shown in Fig. 12. When the normal load is 200 mN, the long and thick chips appear on the as-cast MG surface; while for cases

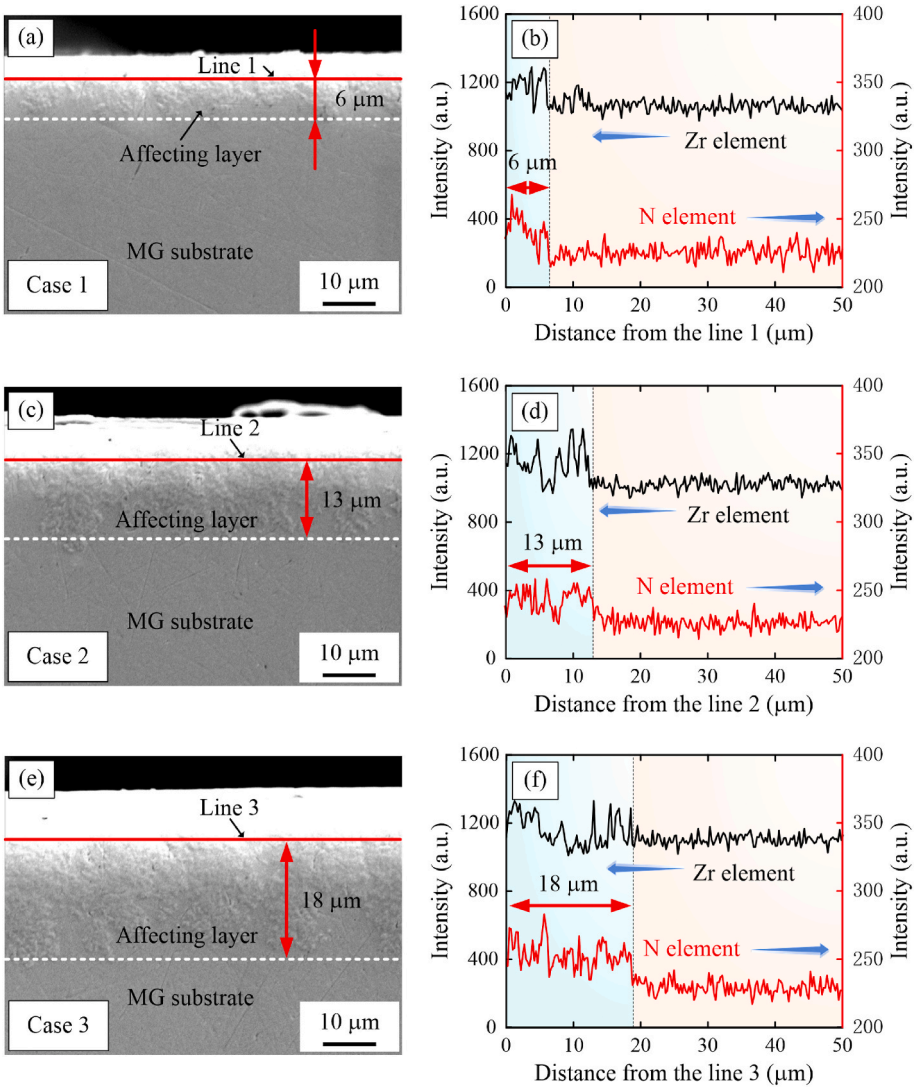

Fig. 10. SEM micrographs of the cross-sections and the corresponding distributions of Zr and N elements along the depth direction of the cross-sections for (a)–(b) case 1, (c)–(d) case 2, and (e)–(f) case 3 surfaces. The lines 1, 2, and 3 correspond to the originations of the EDS line scanning for cases 1, 2, and 3, respectively.

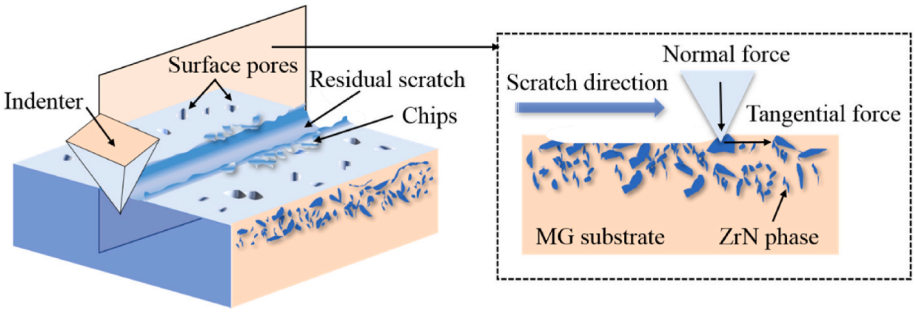

Fig. 11. Schematic diagram illustrating the scratch process on the case 1 surface.

1–3 surfaces, the segmented chips (Fig. 12(c)) or debris (Fig. 12(e) and (g)) are distributed on both sides of the residual scratches. This difference in chip morphology may be ascribed to the combined effects of the following factors: (1) in-situ formed ZrN phase could cause the reduction of removal materials during scratch [45]; (2) the ZrN phase with intrinsic brittleness may cause a rise in brittleness of the laser nitrided surface [46]; (3) discontinuous pores in the laser nitrided surface are likely to cut off the chips and capture partial chips. This can be supported by Fig. 9(b2)-(d2), where the surface pores are almost filled. As the normal load increases to 400 mN, the increasing effect of micro-cutting causes the generation of the chips with large dimension. Especially, for as-cast MG and case 1 surfaces, the continuous strip chips are generated. While for case 2 and case 3 surfaces, although the dimension of the chips is larger than that obtained under the normal load of 200 mN, the chips are still discontinuous.

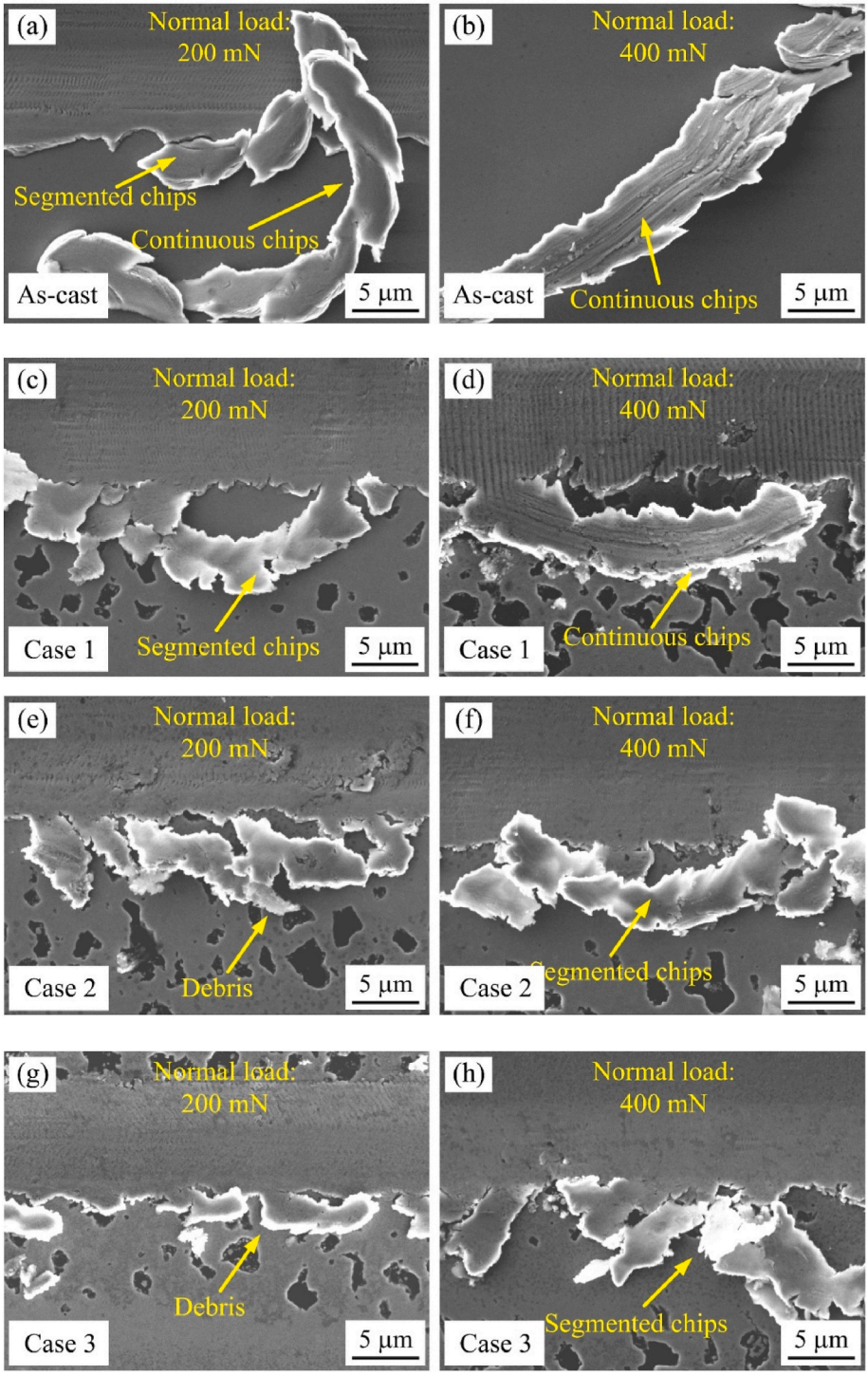

Fig. 12. SEM micrographs of the chips for (a)–(b) as-cast MG, (c)–(d) case 1, (e)–(f) case 2, and (g)–(h) case 3 surfaces under the normal loads of 200 mN and 400 mN.

3.3.3. Coefficient of friction (COF)

To quantitatively evaluate the scratch resistance of the as-cast MG and cases 1–3 surfaces, a comparative analysis of the coefficient of friction (COF) is performed. Accordingly, the COF curves in the stable stage for as-cast MG and cases 1–3 surfaces under various normal loads are illustrated in Fig. 13(a)-13(f), and the corresponding average COFs are summarized in Fig. 13(g). It is observed that regardless of the normal load, the average COFs for cases 1–3 surfaces are always less than that of the as-cast MG, and the average COF gradually decreases from case 1 to case 3. For instance, when the normal load reaches 50 mN, the COFs for as-cast MG, case 1, case 2, and case 3 surfaces are 0.103, 0.073, 0.036, and 0.029, respectively (Fig. 13(g)). That is, the COFs for case 1, case 2, and case 3 surfaces are reduced by 29.12%, 65.05%, and 71.84% in comparison with the as-cast MG. This indicates that scratch resistance is increased from as-cast MG to case 1, case 2, and case 3 surfaces, which matches well with the above analysis on the 3D topographies (Fig. 6) and SEM micrographs (Fig. 9) of the residual scratches. As motived above, compared with the as-cast MG, the reduction in the average COF is primarily ascribed to ZrN phase which reduces the direct load subjected by the MG substrate, and the surface pores may contribute to the

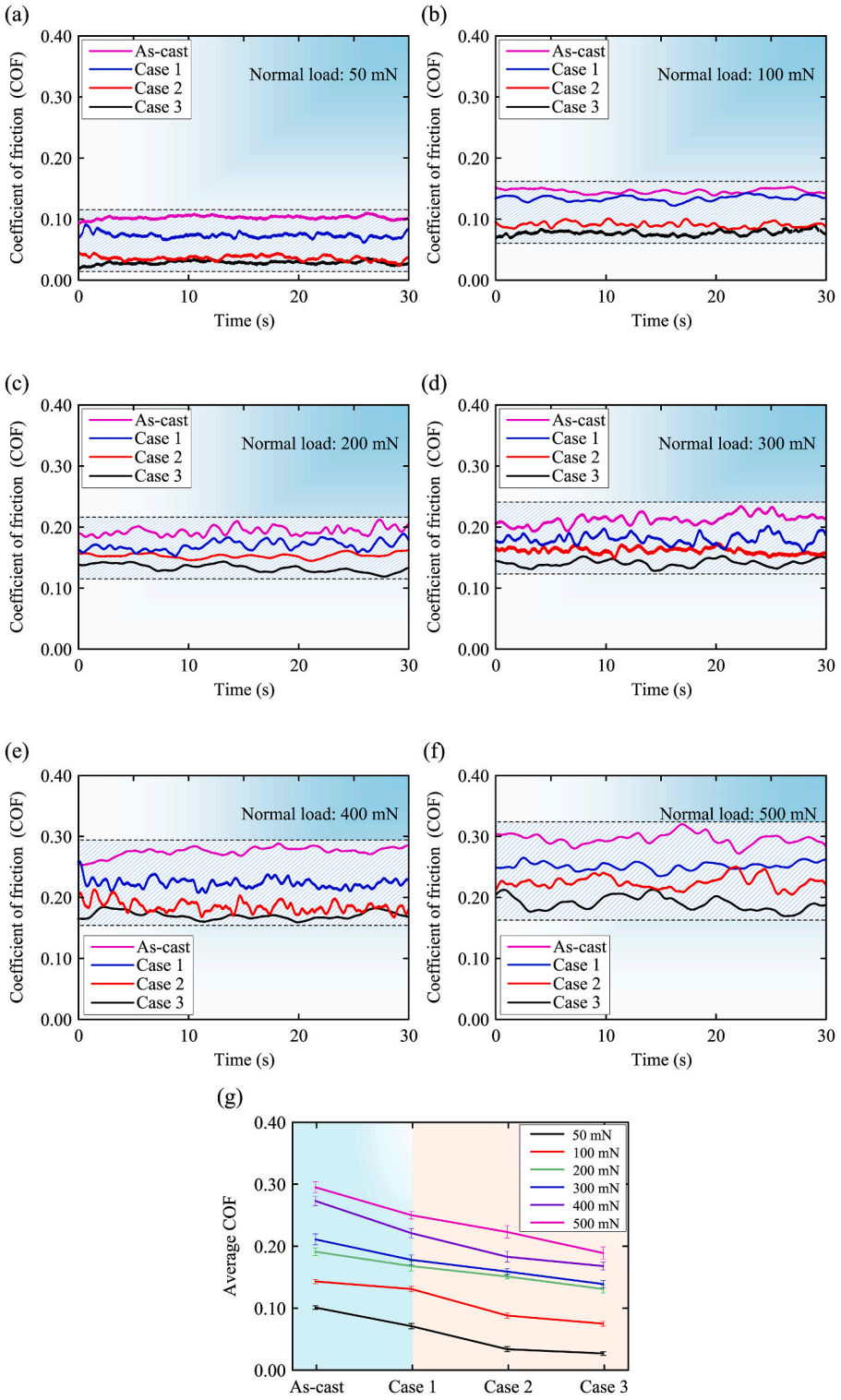

Fig. 13. COF curves for as-cast MG and cases 1–3 surfaces under the normal loads of (a) 50 mN, (b) 100 mN, (c) 200 mN, (d) 300 mN, (e) 400 mN, and (f) 500 mN. (g) presents the average COFs under various conditions.

further reduction in the average COF due to the decrease in the volume of materials around indenter tip.

On the other hand, there are some similarities in the COF curves and average COFs between the as-cast MG and cases 1–3 surfaces. Firstly, all the COF curves exhibit some fluctuations, which get more pronounced as the normal load increases. This fluctuation behavior may be related to the plastic deformation and generation of chips in the scratch region [47,48]. As a chipping event occurs or plastic deformation intensifies, the scratch indenter tends to lose balance and support, leading to a decline in the tangential force. Subsequently, owing to the material resistance and the surface roughness caused by the chips, a relatively high tangential force is required to keep indenter tip moving forward. Thus, a fluctuated COF curve is presented. Combined with the above analysis, the relatively stable COF curves for as-cast MG and cases 1–3 surfaces in Fig. 13(a) are mainly owing to the slight plastic deformation without the chips (Fig. 9(a1)-9(d1)). When increasing the normal load

from 100 mN to 500 mN, the plastic deformation aggravates and the dimension of the chips increases, leading to more pronounced fluctuations in the COF curves in Fig. 13(b)-13(f). Secondly, the average COFs tend to increase with the increase of the normal load from 50 mN to 500 mN (0.103to 0.279 for as-cast MG, 0.073 to 0.252 for case 1, 0.036 to 0.225 for case 2, 0.029 to 0.191 for case 3). This could be owing to that the materials around the indenter tip are severely accumulated at the relatively large normal load. Thus, the tangential force increases accordingly to overcome the larger material resistance [39,41,49]. Nevertheless, laser nitriding has successfully improved the scratch resistance of MG and significantly reduced the COF, which could contribute to the extension of its service life.

4. Conclusions

In summary, by laser nitriding, three types of laser nitrided Zr-based MG surfaces with different surface hardness were prepared. Then, a systematic investigation on the tribological characteristics of these three laser nitrided surfaces was performed by scratch tests. By experiments and analysis, the following conclusions could be obtained.

(1) After performing laser nitriding on the Zr-based MG surface with the selected laser parameters, its hardness had been improved from 6.32 GPa (as-cast MG) to 9.35 GPa (case 1), 13.56 GPa (case 2), and 17.19 GPa (case 3).
(2) Under a given normal load, the cases 1–3 surfaces presented narrower residual scratches as well as less chips and pileups compared with the as-cast MG.
(3) Compared with the as-cast MG, the average COFs for case 1, case 2, and case 3 surfaces were reduced by 29.12% (from 0.103 to 0.073), 65.05% (from 0.103 to 0.036), 71.84% (from 0.103 to 0.029), respectively.
(4) The difference in scratch characteristics between the as-cast MG and laser nitrided surfaces was due to the in-situ formed ZrN phase as well as the surface pores.

Credit author statement

JH: Investigation, Formal analysis, Data curation, Writing – original draft. HW: Investigation, Data curation. HH: Conceptualization, Data curation, Funding acquisition, Methodology, Resources, Supervision, Writing – review & editing. LZ: Data curation, writing-review and editing. ZZ: Data curation. MJ: Investigation. JY: Supervision.

Declaration of competing interest

The authors declare that they have no known competing financial interests or personal relationships that could have appeared to influence the work reported in this paper.

Data availability

Data will be made available on request.

Acknowledgements

This work was supported by National Natural Science Foundation of China (Grant No. 52075221), the Natural Science Foundation of Jilin Province (20220101198JC), National Outstanding Youth Science Fund Project (No. 12125206) of NSFC, and the Fundamental Research Funds for the Central Universities (2020–2023).

References

[1] A. Inoue, A. Takeuchi, Recent progress in bulk glassy alloys, Mater. Trans. 43 (2002) 1892–1906, https://doi.org/10.2320/matertrans.43.1892.
[2] M.M. Trexler, N.N. Thadhani, Mechanical properties of bulk metallic glasses, Prog. Mater. Sci. 55 (2010) 759–839, https://doi.org/10.1016/j.pmatsci.2010.04.002.
[3] B.A. Sun, W.H. Wang, The fracture of bulk metallic glasses, Prog. Mater. Sci. 74 (2015) 211–307, https://doi.org/10.1016/j.pmatsci.2015.05.002.
[4] H.S. Arora, H.S. Grewal, H. Singh, S. Mukherjee, Zirconium based bulk metallic glass-Better resistance to slurry erosion compared to hydroturbine steel, Wear 307 (2013) 28–34, https://doi.org/10.1016/j.wear.2013.08.016.
[5] M.W. Chen, A brief overview of bulk metallic glasses, NPG Asia Mater. 3 (2011) 82–90, https://doi.org/10.1038/asiamat.2011.30.
[6] A. Inoue, A. Takeuchi, Recent development and application products of bulk glassy alloys, Acta Mater. 59 (2011) 2243–2267, https://doi.org/10.1016/j.actamat.2010.11.027.
[7] M.Z. Ma, R.P. Liu, Y. Xiao, D.C. Lou, L. Liu, Q. Wang, Wear resistance of Zr-based bulk metallic glass applied in bearing rollers, Mater Sci Eng A 386 (2004) 326–330, https://doi.org/10.1016/j.msea.2004.07.054.
[8] Q. Halim, N.A.N. Mohamed, M.R.M. Rejab, W.N.W.A. Naim, Q. Ma, Metallic glass properties, processing method and development perspective: a review, Int. J. Adv. Manuf. Technol. 112 (2021) 1231–1258, https://doi.org/10.1007/s00170-020-06515-z.
[9] S.M. Dezfuli, M. Sabzi, Deposition of ceramic nanocomposite coatings by electroplating process: a review of layer-deposition mechanisms and effective parameters on the formation of the coating, Ceram. Int. 45 (2019) 21835–21842, https://doi.org/10.1016/j.ceramint.2019.07.190.
[10] Y.L. An, S.J. Li, G.L. Hou, X.Q. Zhao, H.D. Zhou, J.M. Chen, Mechanical and tribological properties of nano/micro composite alumina coatings fabricated by atmospheric plasma spraying, Ceram. Int. 43 (2017) 5319–5328, https://doi.org/10.1016/j.ceramint.2017.01.072.
[11] K. Derelizade, F. Venturi, R.G. Wellman, A. Kholobysov, T. Hussain, Wear performance of graphene nano plateles incorporated WG-Go coatings deposited by hybrid high velocity oxy fuel thermal spray, Wear (2021) 482–483, https://doi.org/10.1016/j.wear.2021.203974, 203974.
[12] C.G. Tang, Y. Li, K.Y. Zeng, Characterization of mechanical properties of a Zr-based metallic glass by indentation techniques, Mater Sci Eng A 384 (2004) 215–223, https://doi.org/10.1016/J.MSEA.2004.06.013.
[13] H. Huang, M.Q. Jiang, J.W. Yan, The coupling effects of laser thermal shock and surface nitridation on mechanical properties of Zr-based metallic glass, J. Alloys Compd. 770 (2018) 864–874, https://doi.org/10.1016/j.jallcom.2018.08.195.
[14] J. Hong, Y.F. Qian, L. Zhang, H. Huang, M.Q. Jiang, J.W. Yan, Laser nitriding of Zr-based metallic glass: an investigation by orthogonal experiments, Surf. Coat. Technol. 424 (2021), 127657, https://doi.org/10.1016/j.surfcoat.2021.127657.
[15] C.L. Donaghy, R. McFadden, S. Kelaini, L. Carson, A. Margariti, C.W. Chan, Creating an antibacterial surface on beta TNZT alloys for hip implant applications by laser nitriding, Opt Laser. Technol. 121 (2020), 105793, https://doi.org/10.1016/j.optlastec.2019.105793.
[16] P. Schaaf, M. Han, K.-P. Lieb, E. Carpene, Laser nitriding of iron with laser pulses from femtosecond to nanosecond pulse duration, Appl. Phys. Lett. 80 (2002) 1091–1093, https://doi.org/10.1063/1.1448167.
[17] F. Weng, H.J. Yu, C.Z. Chen, J.J. Dai, Microstructures and wear properties of laser cladding Co-based composite coatings on Ti–6Al–4V, Mater. Des. 80 (2015) 174–181, https://doi.org/10.1016/j.matdes.2015.05.005.
[18] J.L. Chen, J. Li, R. Song, L.L. Bai, J.Z. Shao, C.C. Qu, Effect of the Scanning speed on microstructural evolution and wear behaviors of laser cladding NiCrBSi composite coatings, Opt Laser. Technol. 72 (2015) 86–99, https://doi.org/10.1016/j.optlastec.2015.03.015.
[19] G.P. Zhao, C.D. Cho, J.D. Kim, Application of 3-D finite element method using Lagrangian formulation to dilution control in laser cladding process, Int. J. Mech. Sci. 45 (2003) 777–796, https://doi.org/10.1016/S0020-7403(03)00140-1.
[20] W.Y. Yuan, R.F. Li, Z.H. Chen, J.Y. Gu, Y.T. Tian, A comparative study on microstructure and properties of traditional laser cladding and high-speed laser cladding of Ni45 alloy coatings, Surf. Coat. Technol. 405 (2021), 126582, https://doi.org/10.1016/j.surfcoat.2020.126582.
[21] J.J. Dai, C.Z. Chen, S.Y. Li, L. Zhuang, Microstructure and properties of laser surface carburized Titanium and Titanium alloys, Adv. Mater. Res. 936 (2014) 1086–1090. https://doi.org/10.4028/www.scientific.net/AMR.936.1086.
[22] A.F. Saleh, J.H. Abboud, K.Y. Benyounis, Surface carburizing of Ti–6Al–4V alloy by laser melting, Opt Laser. Eng. 48 (2010) 257–267, https://doi.org/10.1016/j.optlaseng.2009.11.001.
[23] T.T. Xu, W. Shi, C.R. Zhao, Y.Y. Zhou, Y.C. Shi, Study on mechanism of improving wear and corrosion properties of 20CrMnTi ring gear surface by laser carburizing, Mater. Today Commun. 32 (2022), 104029, https://doi.org/10.1016/j.mtcomm.2022.104029.
[24] H. Huang, M.Q. Jiang, J.W. Yan, Softening of Zr-based metallic glass induced by nanosecond pulsed laser irradiation, J. Alloys Compd. 754 (2018) 215–221, https://doi.org/10.1016/j.jallcom.2018.04.278.
[25] M.C. Li, M.Q. Jiang, F. Jiang, L. He, J. Sun, Testing effects on hardness of a Zr-based metallic glass under nanoindentation, Scripta Mater. 138 (2017) 120–123, https://doi.org/10.1016/j.scriptamat.2017.05.046.
[26] L. Wang, W. Lu, Y.F. Xue, H.F. Zhang, H.M. Fu, Nanoindentation response of laser shock peened Ti-based bulk metallic glass, AIP Adv. 5 (2015) 1947, https://doi.org/10.1063/1.4921898.
[27] G.Y. Deng, A.K. Tieu, L.H. Su, H.T. Zhu, Q. Zhu, W.F.H. Zamri, C. Kong, Characterizing deformation behaviour of an oxidized high speed steel: effects of nanoindentation depth, friction and oxide scale porosity, Int. J. Mech. Sci. 155 (2019) 267–285, https://doi.org/10.1016/j.ijmecsci.2019.02.043.

[28] W.C. Oliver, G.M. Pharr, An improved technique for determining hardness and elastic modulus using load and displacement sensing indentation experiments, J. Mater. Res. 7 (1992) 1564–1583.
[29] J. Dong, M. Gao, Y. Huan, Y.H. Feng, W. Liu, W.H. Wang, Enhanced tensile plasticity of Zr based bulk metallic glasses by a stress induced large scale flow, J. Alloys Compd. 727 (2017) 297–303, https://doi.org/10.1016/j.jallcom.2017.08.046.
[30] J.L. Cheng, G. Chen, W. Zhao, Z.Z. Wang, Z.W. Zhang, Enhancement of tensile properties by the solid solution strengthening of nitrogen in Zr-based metallic glass composites, Mater Sci Eng A 696 (2017) 461–465, https://doi.org/10.1016/j.msea.2017.04.075.
[31] L. Deng, K. Kosiba, R. Limbach, L. Wondraczek, U. Kühn, S. Pauly, Plastic deformation of a Zr-based bulk metallic glass fabricated by selective laser melting, J. Mater. Sci. Technol. 60 (2021) 139–146, https://doi.org/10.1016/j.jmst.2020.06.007.
[32] S. Ulrich, C. Ziebert, M. Stqber, E. Nold, H. Holleck, M. Gfken, E. Schweitzer, P. Schlogmacher, Correlation between constitution, properties and machining performance of TiN/ZrN multilayers, Surf. Coating. Technol. 188 (2004) 331–337, https://doi.org/10.1016/j.surfcoat.2004.08.056.
[33] X.M. Cui, Z.L. Yu, F. Liu, Z.X. Du, P.C. Bai, Influence of secondary phases on crack initiation and propagation during fracture process of as-cast Mg-Al-Zn-Nd alloy, Mater Sci Eng A 759 (2019) 708–714, https://doi.org/10.1016/j.msea.2019.05.062.
[34] C.A. Schuh, T.C. Hufnagel, U. Ramamurty, Mechanical behavior of amorphous alloys, Acta Mater. 55 (2007) 4067–4109, https://doi.org/10.1016/j.actamat.2007.01.052.
[35] S. Yoon, J. Kim, B.D. Kim, C. Lee, Tribological behavior of B4C reinforced Fe-base bulk metallic glass composite coating, Surf. Coating. Technol. 205 (2010) 1962–1968, https://doi.org/10.1016/j.surfcoat.2010.08.078.
[36] J.W. Qiao, H.L. Jia, P.K. Liaw, Metallic glass matrix composites, Mater. Sci. Eng. R Rep. 100 (2016) 1–69, https://doi.org/10.1016/j.mser.2015.12.001.
[37] P. Gong, F.W. Li, L. Deng, X.Y. Wang, J.S. Jin, Research on nano-scratching behavior of TiZrHfBeCu(Ni) high entropy bulk metallic glasses, J. Alloys Compd. 817 (2020), 153240, https://doi.org/10.1016/j.jallcom.2019.153240.
[38] T. Ayyagari, W. Scharf, S. Mukherjee, Dry reciprocating sliding wear behavior and mechanisms of bulk metallic glass composites, Wear 350–351 (2016) 56–62, https://doi.org/10.1016/j.wear.2016.01.003.
[39] C. Su, X.H. Sang, S.J. Niu, R.M. Ren, A comparison of the abrasive wear behaviors of cast iron and cast steel materials, J. Mater. Eng. Perform. 30 (2021) 4572–4582, https://doi.org/10.1007/s11665-021-05758-5.
[40] X.J. Xu, V. Sybrand, W. Xu, The effect of martensite volume fraction on the scratch and abrasion resistance of a ferrite–martensite dual phase steel, Wear 348–349 (2016) 80–88, https://doi.org/10.1016/j.wear.2015.11.017.
[41] C.T. Pan, T.T. Wu, C.F. Liu, C.Y. Su, W.J. Wang, J.C. Huang, Study of scratching Mg-based BMG using nanoindenter with Berkovich probe, Mater Sci Eng A 527 (2010) 2342–2349, https://doi.org/10.1016/j.msea.2009.11.070.
[42] M. Das, V.K. Balla, D. Basu, S. Bose, A. Bandyopadhyay, Laser processing of SiC-particle-reinforced coating on titanium, Scripta Mater. 63 (2010) 438–441, https://doi.org/10.1016/j.scriptamat.2010.04.044.
[43] C.C. Wang, G.Q. Zhang, Z.P. Li, X.Q. Zeng, Y. Xu, S.C. Zhao, H.X. Hu, Y.D. Zhang, T.H. Ren, Tribological behavior of Ti-6Al-4V against cortical bone in different biolubricants, J Mech Behav Biomed 90 (2019) 460–471, https://doi.org/10.1016/j.jmbbm.2018.10.031.
[44] C.C. Wang, Z.P. Li, H. Zhao, G.Q. Zhang, T.H. Ren, Y.D. Zhang, Enhanced anticorrosion and antiwear properties of Ti–6Al–4V alloys with laser texture and graphene oxide coatings, Tribol. Int. 152 (2020), 106475, https://doi.org/10.1016/j.triboint.2020.106475.
[45] Y.J. Huang, Y.L. Chiu, J. Shen, Y. Sun, J. Chen, Mechanical performance of metallic glasses during nanoscratch tests, Intermetallics 18 (2010) 1056–1061, https://doi.org/10.1016/j.intermet.2010.02.002.
[46] J. Chen, M.R. Geng, Y.Q. Li, Z.F. Yang, Y. Chai, G.Y. He, Erosion resistance and damage mechanism of TiN/ZrN nanoscale multilayer coating, Coatings 9 (2019), 103390, https://doi.org/10.3390/coatings9020064.
[47] D. Lahiri, J. Karp, A.K. Keshri, C. Zhang, G.S. Dulikravich, L.J. Kecskes, A. Agarwal, Scratch induced deformation behavior of hafnium based bulk metallic glass at multiple load scales, J. Non-Cryst. Solids 410 (2015) 118–126, https://doi.org/10.1016/j.jnoncrysol.2014.12.010.
[48] J. Liu, H. Jiang, Q. Cheng, C.M. Wang, Investigation of nano-scale scratch and stick-slip behaviors of polycarbonate using atomic force microscopy, Tribol. Int. 125 (2018) 59–65, https://doi.org/10.1016/j.triboint.2018.04.024.
[49] A.M. Hodge, T.G. Nieh, Evaluating abrasive wear of amorphous alloys using nanoscratch technique, Intermetallics 12 (2004) 741–748, https://doi.org/10.1016/j.intermet.2004.02.014.